Size dependence of mechanical properties of gold at the micron scale in the absence of strain gradients

Julia R. Greer [a],*, Warren C. Oliver [b], William D. Nix [a]

[a] *Department of Materials Science and Engineering, Stanford University, 416 Escondido Mall, Stanford, CA 94305-2205, USA*
[b] *MTS Nano Innovation Center, Oak Ridge, TN 37830, USA*

Abstract

Classical laws of mechanics hold that mechanical properties are independent of sample size; however, results of experiments and molecular dynamics simulations indicate that crystals exhibit strong size effects at the sub-micron scale. In experimental studies, the size effect can be explained by strain gradients. Atomistic simulations suggest that the yield strength depends on the size even without strain gradients and scales with the sample size through a power relationship. We address these different approaches to the size dependence of mechanical properties. Results of uniaxial compression experiments on gold at the sub-micron scale, without stress/strain gradients, are presented here. Freestanding Au cylinders are created by two unique fabrication processes and subsequently compressed in the Nanoindenter with a flat punch. Compressive stress, strain, and stiffness of the pillars are determined. Test results indicate a significant flow stress increase, up to several GPa. These high strengths appear to be controlled by dislocation starvation, unique to small crystals.
© 2005 Acta Materialia Inc. Published by Elsevier Ltd. All rights reserved.

Keywords: Size effect; Plasticity; Micron scale; Strain gradients

1. Introduction

Investigations of a characteristic length scale associated with the widely observed increase in strength with decreasing sample size date back to 1994 when Fleck et al. [1] described a series of experiments on yielding of copper wires in tension and torsion. In this study, higher flow stresses were observed for smaller-diameter wires when tested in torsion compared to tension. The ideas in this paper initiated a burst of experimental studies on size-dependent mechanical properties. Stolken and Evans [2] reported higher strengths for thinner Ni foils subjected to the same bending conditions as thicker ones. Results of numerous nanoindentation experiments in 1993–1999 conducted by Stelmashenko et al. [3], De Guzman et al. [4], Atkinson [5], Ma and Clarke [6], Poole et al. [7], McElhaney et al. [8] and Suresh et al. [9] showed a very strong inverse relationship between the hardness and the indentation depth or size of the indentation. The one similarity among the experimental studies mentioned above is the presence of strain gradients in the deformation process. In nanoindentation experiments, for example, plastic deformation is confined within a very small volume. This results in the creation of non-uniform stresses and strains within the sample, thereby setting up strong gradients of strain, which are thought to be responsible for the so-called indentation size effect (ISE) [10–17]. The observed ISE can be explained in part by the strain gradient plasticity theory developed by Nix and Gao [11], which predicts a linear relationship between the square of the indentation hardness and the reciprocal of the indentation depth.

* Corresponding author. Tel.: +1 415 265 8537; fax: +1 650 725 4034.
   E-mail address: jrosolov@alum.mit.edu (J.R. Greer).

The model utilizes Taylor's relation between the flow stress and the dislocation density and makes use of the concept of the evolving density of the so-called "geometrically necessary" dislocations [12]. The Nix–Gao model, however, is continuum-based and therefore cannot predict the observed discrete displacement bursts characteristic of the elastic-to-plastic transition at indentation depths less than ~100 nm [19–24]. The discrete displacement bursts found in single crystalline materials during the initial stages of nanoindentation are most likely associated with the nucleation of dislocations, the primary mechanism of plasticity on the nanometer scale.

In addition to the studies of length scale effects in bulk materials, many investigations of thin film mechanical properties have been carried out. Higher strengths observed in thin metal films relative to their bulk counterparts are usually attributed to the confinement of dislocations within the film by the presence of the substrate and in some cases the passivation, as well. This concept was first discussed by Frank and van der Merwe [25], then developed by Matthews and Blakeslee [26,27], and later fully developed by Freund [28] and modified for metal films by Nix [29]. These M–B–F–N models showed that the strength of thin films scales inversely with film thickness. Although the models derived by Matthews and Blakeslee, Freund and Nix give a good account of the motion of isolated dislocations in thin films, they do not account for discrete nucleation events or for interactions of dislocations with other imperfections. Plastic deformation of polycrystalline thin metal films has also been investigated by Blanckenhagen et al. [30] with the help of a discrete dislocation dynamics simulation of a Frank–Read source operating in the confined geometry of a thin film on a substrate. This model predicts a flow stress that scales inversely with the film thickness or grain size (whichever is smaller) and that is roughly four times higher than predicted by previous models, thereby giving better agreement with TEM studies [31]. While these studies of thin films constitute important size effects for plasticity, they arise from the constraining effects of surrounding layers. In the present work we focus our attention on size effects that arise in unconstrained geometries.

An alternative approach for unconstrained plasticity was taken by Horstemeyer et al. [32], who performed atomistic simulations of plasticity via the embedded atom method (EAM). In these molecular dynamics simulations, the energy of embedding an atom into a computational cell is calculated as a function of the local electron density and a repulsive pairwise potential. The flow stresses are then calculated based on the volume average of these forces in response to a known shear deformation. The results of these simulations indicated that plastic deformation is intrinsically inhomogeneous, that the yield strength depends on the sample size even

in the absence of strain gradients, and that for small single crystals, the yield strength scales inversely with the volume-to-surface area ratio of the sample.

This brief review shows that there are at least two rather different approaches that have been developed to explain the observation of higher strengths in smaller volumes of material when not constrained by surrounding materials. In one set of explanations, the higher strengths are linked to the strong gradients of strain that accompany deformation is such small volumes. In the other approach, the high strengths are associated the dislocation starved conditions that prevail in small volumes, causing the nucleation of dislocations to dominate the plastic resistance. While all of these studies are consistent with the tenet that smaller is stronger, a unified plasticity mechanism is yet to be established.

2. Experimental

In order to gain insight into the deformation mechanisms responsible for plasticity at the micron scale, we have designed and executed experiments for testing the elastic and plastic properties of gold in the absence of the strong gradients of strain usually associated with micron scale deformation. The test methodology includes the fabrication of single-crystalline and polycrystalline free-standing gold cylinders (pillars) of sub-micron dimensions using two distinct fabrication processes. The uniaxial deformation properties of these pillars are studied via micro-compression testing techniques. As described below, we have developed both a focused ion beam (FIB) machining technique and an IC fabrication process for creating sub-micron sized pillars of gold. We have also developed uniaxial testing techniques for studying the mechanical properties of these tiny samples. We are able to conduct uniaxial compression tests on pillars of varying sizes and aspect ratios using the MTS Nanoindenter XP with a custom-machined flat punch diamond tip.

2.1. Fabrication processes – focused ion beam machining vs. electroplating

We have developed two distinct fabrication processes for sample manufacturing to ensure that the observed effects are not linked to a specific fabrication technique. The first employs the FIB to etch patterns of interest into single crystal gold discs while the second utilizes the Stanford Nanofabrication Facility (SNF) for lithography-governed processing. Following the approach used by Uchic et al. [33], a 'focused ion beam fabrication approach' has been developed to create sub-micron pillars of gold using a ⟨0 0 1⟩-oriented single crystal gold disc as a precursor for pillar fabrication. The present work extends the FIB fabrication technique for the first

time to gold, without a surface oxide, and to much smaller pillars than those described by Uchic et al. [33]. Initially, a high current of Ga ions of 3000 pA in the FIB is used to mill out a crater in the material leaving a 4 μm-diameter "island" in the center. It is important to fabricate the pillar in a crater to guarantee that the indenter tip is in contact only with the pillar of interest. Finer currents and various tilt angles are then used to refine this structure into a ∼3:1 aspect ratio upright gold pillar with a flat top. Some representative examples of FIB'd gold pillars are shown in Fig. 1.

In the microfabrication approach, a standard $\langle 1\,0\,0 \rangle$ Si substrate is coated with low-stress Si_3N_4 on both sides as a diffusion barrier layer. Then, 250 nm of Ti/TiN is sputter-deposited onto the wafer to serve as a conductive yet non-reflective layer for further processing. Then a 3 μm-thick layer of photoresist is spun onto the wafer, baked, and exposed in the Nikon G-line stepper. We designed a mask pattern to image isolated contact holes ranging from 0.8 to 1.2 μm in diameter while maintaining small separation distances between the contact holes for better proximity correction. After the post-exposure bake, the contact holes are developed and dry etched in an O_2 plasma to enhance straight wall uniformity. The gold is then electrodeposited into the holes from the revealed TiN circles. Electrodeposition techniques, however, produce very fine-grained microstructures, and since we are mainly interested in single-crystal deformation, it is necessary to further anneal the as-deposited gold pillars. The photoresist has to be stripped prior to this anneal since it cannot withstand high temperatures needed for grain growth. A fully encapsulating matrix of PVD SiO_2 is then deposited over the entire wafer for pillar shape retention at high temperature. After annealing the matrix at 400 °C for 4 h, the sample is wet etched in 6:1 HF to reveal large arrays of free-standing gold pillars. Some examples of the electroplated pillars are shown in Fig. 2.
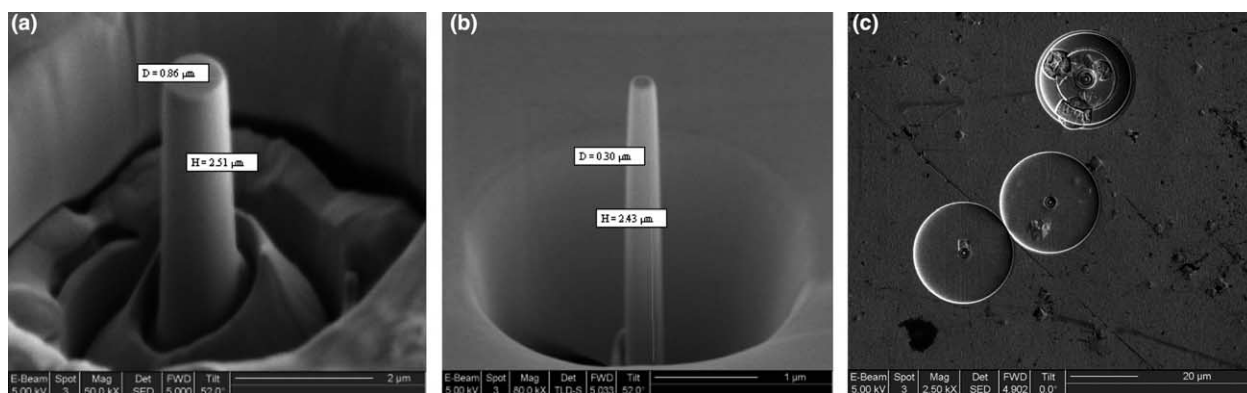

Fig. 1. (a) FIB image of a 860 nm-diameter, 3.2 μm-tall $\langle 0\,0\,1 \rangle$ gold pillar; (b) FIB image of a 300 nm-diameter, 3.15 μm-tall $\langle 0\,0\,1 \rangle$ gold pillar; (c) top view of the "donut holes".
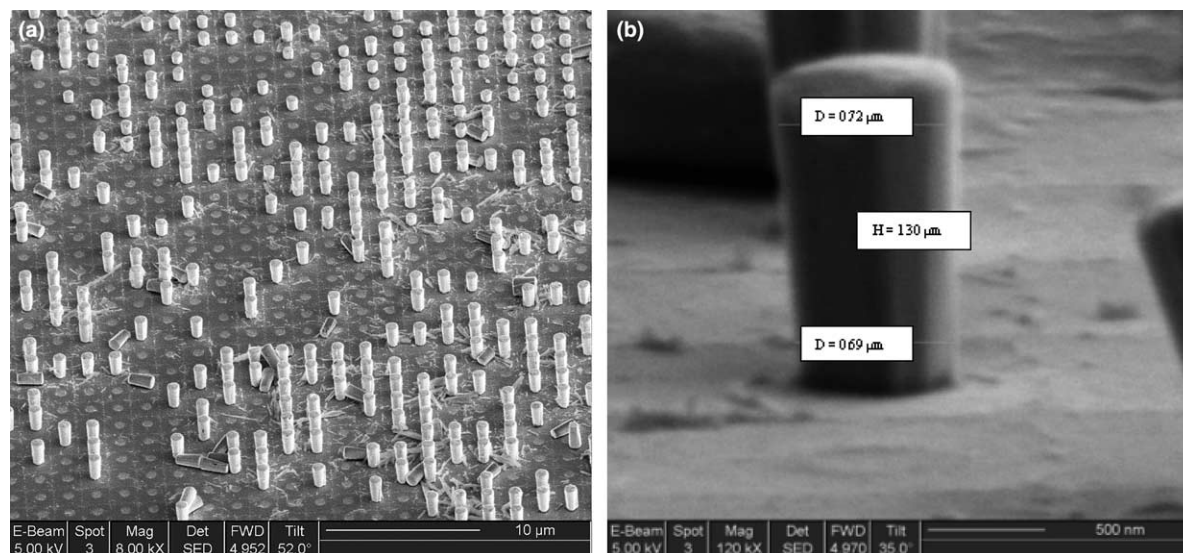

Fig. 2. (a) SEM image of an array of electroplated gold pillars at 52° tilt; (b) as-deposited single pillar.

2.2. Mechanical testing

All pillars were compressed using the dynamic contact module of the Nanoindenter XP with a flat punch indenter tip at Stanford University. The flat punch tip was custom machined out of a standard Berkovich indenter by etching off the diamond tip in the FIB, resulting in the projected area of an equilateral triangle with a 9 μm inscribed circle diameter. The indenter system is thermally buffered from its surroundings to within 1 °C; however, small temperature fluctuations cause some of the machine components to expand and contract, and this change is manifested in the data as an apparent displacement in the specimen. To account for thermal drift, the rate of displacement was measured in the final 100 s of the hold period, and the displacement data were corrected by this drift amount. It is important to recognize that this method for drift correction assumes that the displacement fluctuations during the hold time were mainly due to the thermal drift rather than to creep of the gold pillars. The validity of this assumption comes from the result that the load–displacement data prior to the correction is within 2 nm of that after the correction.

Most experiments were performed using multiple cycles of loading/unloading before reaching the maximum load in order to ensure that the unloading data was indeed elastic. In each experiment, the indenter was loaded and unloaded at least twice while maintaining a constant nominal strain rate of $0.004\,\mathrm{s}^{-1}$, with each of the unloading sections terminated at 10% of the hold load to ensure the presence of the contact. Load–displacement data were collected in the continuous stiffness measurement (CSM) mode of the instrument. The experimental procedure involved first, locating the pillar of choice under the top-view 150X optical microscope, then calibrating the indenter to microscope distance to within a fraction of a micron on the surface of the sample away from the pillars, and finally moving the calibrated flat indenter tip to the position directly above the specimen. Thermal drift stabilization is then followed by compressing the pillar at a constant nominal strain rate. During the initial segment of the test, the instrument locates the sample surface and then moves to the specified location and starts the initial approach segment, decreasing the approach velocity to 5 nm/s when the indenter is less than 6 m above the surface. Once the surface of the pillar has been detected, such parameters as the force on the pillar, harmonic contact stiffness, and the compressive displacement of the top of the pillar from the point of contact are continuously measured and recorded. These and some other parameters of interest like unloading stiffness and modulus can then be calculated and plotted. The load–displacement data obtained during the compression experiments are then converted to stresses and strains.

2.3. Data analysis

In order to calculate stress and strain, we assume a perfectly cylindrical pillar of height L_0 and cross-sectional area A_0. Upon uniaxial compression, the plastic volume of the cylinder is assumed to be conserved, and the final height and cross-sectional area are L_p and A_p, respectively, such that $A_p L_p = L_0 A_0$. The total strain throughout the deformation can then be represented as the sum of elastic and plastic compressive strains (compressive strains are taken to be positive here)

$$\varepsilon_{\mathrm{TOT}}^{\mathrm{compressive}} = \varepsilon_{\mathrm{el}} + \varepsilon_{\mathrm{pl}} = \frac{1}{E}\frac{PL_p}{A_0 L_0} - \ln\left(\frac{L_p}{L_0}\right), \qquad (1)$$

where P is the instantaneous load on the pillar, E is the elastic modulus of gold in the $\langle 0\,0\,1 \rangle$ orientation, A_0 and L_0 are the original cross-sectional area and height of the pillar, and L_p is the original pillar height less its plastic compressive displacement, u_p. The latter is equal to the difference between the measured total displacement at any point on the loading curve, u, and the elastic displacement, u_{el}, which is derived based on Hooke's law and the assumption of volume conservation during plastic flow

$$u_{\mathrm{el}} = \frac{1}{E}\frac{P}{A_0 L_0} L_p^2. \qquad (2)$$

The plastic displacement, then, is represented by the following expression:

$$u_p = u - \frac{1}{E}\frac{P}{A_0 L_0} L_p^2. \qquad (3)$$

Substituting u_p into the expression for $L_p = L_0 - u_p$ leads to the following relation for L_p:

$$L_p = \frac{EA_0 L_0}{2P}\left(1 - \sqrt{1 - 4\left(\frac{P}{EA_0 L_0}\right)(L_0 - u)}\right), \qquad (4)$$

where P and u are the load and displacement as measured by the Nanoindenter, $L_0 A_0$ is the original volume of the pillar, and E is the elastic modulus of gold along the axis of loading. The total compressive strain is then calculated based on Eq. (1).

The stresses are calculated by dividing the measured load by the plastic area, using the assumption of constant plastic volume for calculating A_p,

$$\sigma = \frac{P}{A_P} = \frac{PA_0 L_0}{L_p}. \qquad (5)$$

A typical load–displacement graph generated by the Nanoindenter and the corresponding stress–strain curve are presented in Fig. 3.

In addition to measuring the load and the length change of the pillar, the Nanoindenter operates in the CSM mode, which enables it to continuously measure the instantaneous stiffness of the specimen. However,
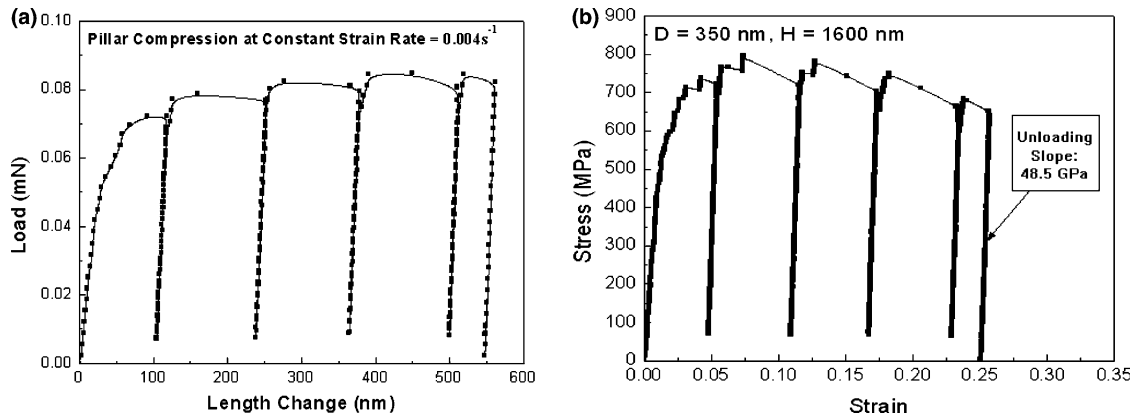
Fig. 3. (a) Compression of a single crystal ⟨0 0 1⟩-oriented FIB'd gold pillar; (b) stress–strain plot generated based on this data.

the overall stiffness, and therefore, compliance reported by the instrument includes the combined effect of the compliance of the pillar itself as well as the compliance associated with the pillar acting like a flat punch indenter, elastically pushing into the bulk of the gold. In order to calculate the true pillar stiffness, this additional indentation compliance has to be removed. Sneddon [34] provided the solution for a perfectly rigid circular flat punch indenting into an isotropic elastic half space in 1965. His expression for contact compliance is given as

$$C_{Sneddon} = \frac{\sqrt{\pi}(1 - v^2)}{2E_{polyX}\sqrt{A_p}}. \qquad (6)$$

Here, E_{polyX} is the polycrystalline elastic modulus of gold, A_p is the instantaneous cross-sectional area of the pillar, and v is the Poisson ratio of gold. The pillar stiffness is then calculated by subtracting this Sneddon compliance ($C_{Sneddon}$) from the inverse of the stiffness measured by the Nanoindenter (S_{meas}).

$$S_{pillar} = \frac{1}{(1/S_{meas}) - C_{Sneddon}}. \qquad (7)$$

These stiffness measurements were then compared to the theoretical stiffness values based on Young's modulus in the ⟨0 0 1⟩ orientation ($E_{⟨0\,0\,1⟩}$), and the calculated instantaneous area (A_p) and length (L_p) derived in Eq. (4).

$$S_{pillar} = \frac{E_{⟨0\,0\,1⟩}A_p}{L_p}. \qquad (8)$$

These theoretical and measured stiffnesses were found to be in very good agreement, as shown in a representative stiffness curve in Fig. 4. The rapid increase in stiffness from 0 to the theoretical value during the initial section of the measured stiffness curve is the result of the imperfect alignment between the indenter and the pillar top at the start of the experiment. Similarly, the two points underneath the main measured stiffness curve correspond to the very short, ∼0.5 s, periods of indenter settling during the two re-loading segments. Stiffness

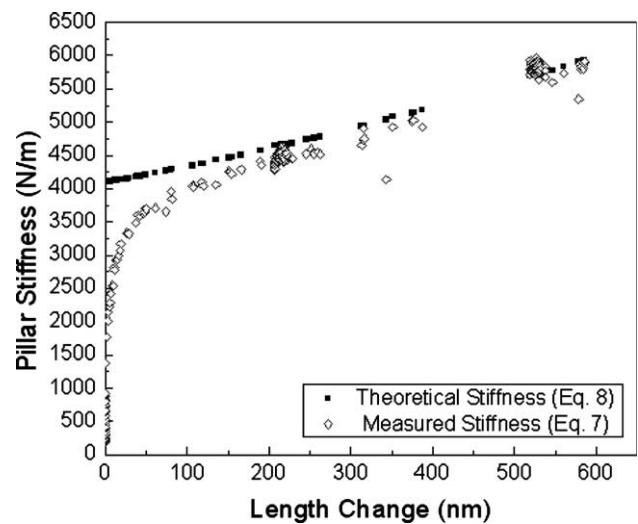Fig. 4. Measured stiffness (Eq. (7)) vs. theoretical stiffness (Eq. (8)) for a ⟨0 0 1⟩-oriented FIB'd pillar.

comparisons of this kind provide strong evidence that the diamond indenter is only making contact with the pillars during these experiments. This, in turn, means that the imposed loads are supported by the pillars only, and that the computed high stresses described below are valid.

3. Compression properties of FIB'd gold pillars

The results of our uniaxial compression experiments indicate a strong sample size effect: pillars made by both fabrication methods yielded at stresses that are much higher than the typical yield strength of bulk gold estimated at 30 MPa at 2% strain [35]. Moreover, the flow stresses for single-crystalline ⟨0 0 1⟩-oriented pillars rapidly increase as their diameters are reduced below 1 μm. A set of stress–strain curves for the various FIB'd pillars is shown in Fig. 5.

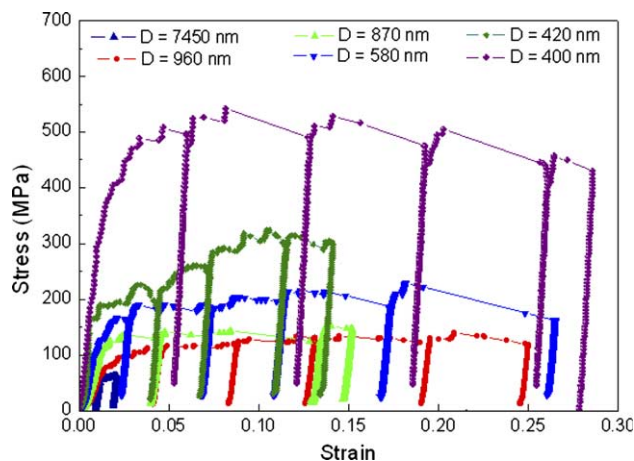Fig. 5. Stress–strain behavior of ⟨0 0 1⟩-oriented FIB'd pillars: flow stresses increase significantly for pillars with a diameter of 500 nm and less.

smaller than some critical diameter, flow stresses at 10% strain vary inversely with the diameter through a very strong function, much stronger than a power law.

SEM analysis indicates that all pillars were deformed by crystallographic slip on {1 1 1}-type planes, as expected. Images representing the same pillar before and after deformation as well as a pillar exhibiting severe multiple slip are shown in Fig. 7. The clear slip lines on the deformed specimen are oriented at approximately 55° from the loading axis matching the calculated value of 54.7° as the angle between ⟨0 0 1⟩ and ⟨1 1 1⟩ zone axes.

As shown in Fig. 5, five different pillars with diameters ranging between 400 and 7450 nm were compressed, and their compressive stress–strain behavior was plotted. As can be seen from the graph, the smallest pillar reaches a compressive stress of 550 MPa at 10% strain. While in some cases the initial stages of deformation are not purely elastic due to the gradual onset of yielding (caused by the imperfect initial alignment between the indenter and the pillar top), the initial loading slopes of the well-aligned tests give elastic moduli very close to the Young's modulus of gold in the ⟨0 0 1⟩ direction, 43 GPa. The fully elastic unloading slopes closely match the expected value, as well. As shown in Fig. 6, for sizes
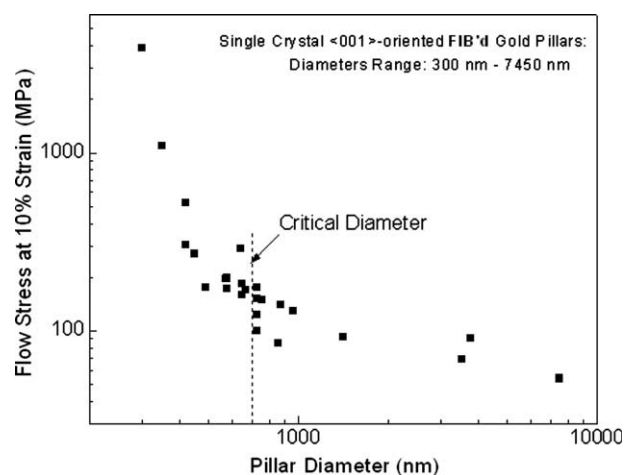

Fig. 6. Flow stress at 10% strain vs. pillar diameter plotted on log–log scale. Flow stresses rapidly increase as the diameter is reduced.
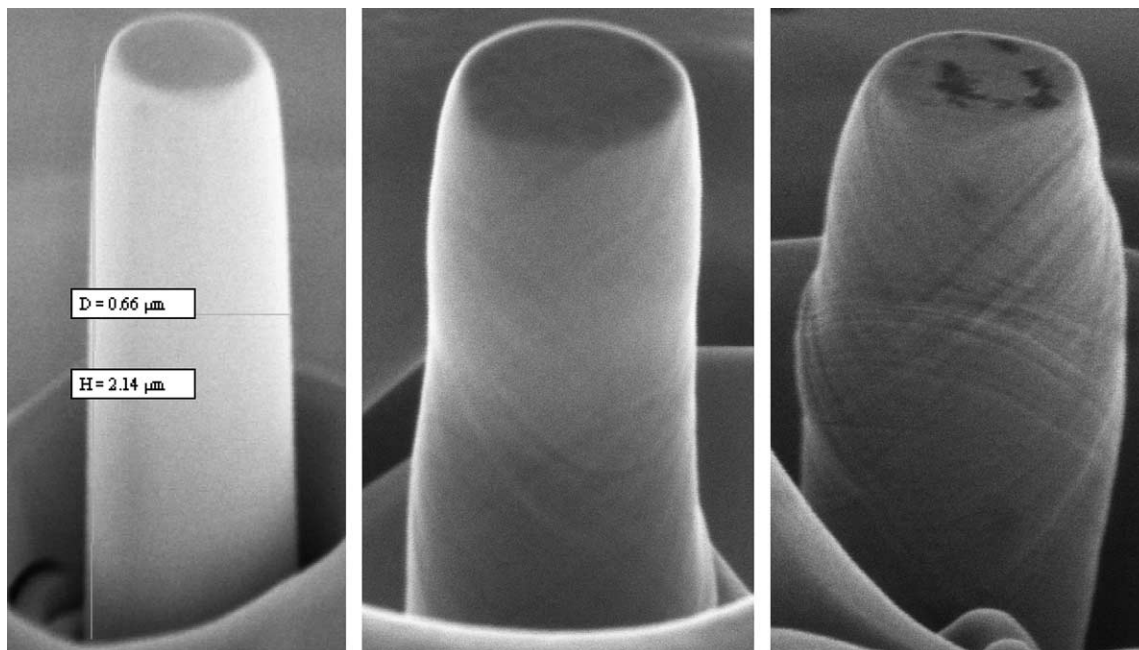

Fig. 7. SEM images of undeformed, deformed, and severely deformed pillars. Slip lines are clearly present in the deformed states.

4. Compression properties of electroplated gold pillars

One of the major concerns with the FIB fabrication technique is the possibility of Ga^+ ion implantation into the sample, which might be responsible for the observed increase in strengths. To address this issue, we have developed an alternative fabrication technique based on lithographic patterning and electroplating, the key steps of which were described in a previous section. These annealed, lithographically patterned pillars also yield at stresses higher than that for bulk gold and, more importantly, exhibit a similar rise in strength as the diameter is reduced. Fig. 8 shows the flow stresses of the electroplated and annealed pillars in comparison with those fabricated via FIB. As expected, the flow stresses of the electroplated pillars are higher than those of the single-crystalline FIB'd pillars since the former are composed of 2–3 grains per pillar. All the grains, however, are continuous across the pillar width, as shown in a representative cross-section of one annealed electroplated pillar in Fig. 8.

In addition to our own experimental results on Ga^+ implantation, several literature sources report that the implantation depths for 30 KeV Ga^+ beam are no greater than 60 nm. Arnold et al. [36] and Machalett et al. [37] independently demonstrated in 2003 that the surface damage from 30 KeV Ga^+ beam on FIB-prepared TEM specimens of Pt, W, and Au penetrated no further than 20–25 nm into the surface of gold when the Ga beam was directed normal to the gold surface. In our fabrication process, even less penetration is expected since the Ga^+ ions strike the sides of the gold pillars at low angles of incidence. Based on the clearly observed size effect in the deformation of the electroplated pillars and on these literature studies, we do not believe that the significant increase in flow stresses of the FIB'd pillars can be attributed to the Ga^+ implantation into the specimen.

4.1. Discussion

The results of all of our experiments indicate that a distinct size effect is present when sub-micron-sized gold pillars are plastically deformed in uniaxial compression. Unlike most of the previous experimental work on size effects in mechanical properties [1–24], the present experiments do not involve significant gradients of strain during the deformation. Inhomogeneous deformation due to barreling of the pillars at large strains occurs after the very high strengths are observed and is not considered to be a major factor in the observed high strengths.

Before discussing possible causes for the observed size effects in the gold nanopillars we should mention the strong size effects on strength that have been observed for thin metal films, either free-standing or on substrates, when deformed in uniaxial tension [38–41]. These experiments are relevant to the present discussion as they were also conducted in the absence of significant strain gradients. Thermal cycling experiments on polycrystalline gold films on silicon substrates, for example, show a strong size effect on room temperature strength [42]. Biaxial strengths as high as 700 MPa were observed for 200 nm thick films. This size effect and the others mentioned here are commonly thought to arise either from the confining effect of the substrate on dislocation motion or the fine grain sizes and twins present in these deposited films. Yu and Spaepen [38] and Hommel and Kraft [39] both studied plastic deformation of Cu films on polyimide substrates in uniaxial tension. They found strong size effects which could be attributed to the fine grain sizes present in these films and to the presence of twins. The film thickness itself also appeared to play a role in these size effects. Huang and Spaepen [40] also showed that ~5 μm-thick free-standing films of silver and copper, deformed in uniaxial tension, were much stronger their bulk counterparts. Most likely this
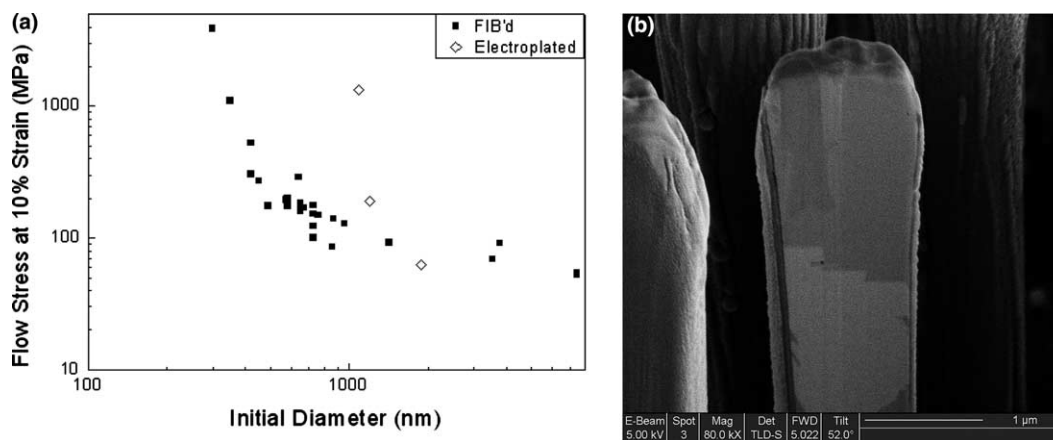

Fig. 8. (a) Flow stress vs. initial diameter for single-crystalline FIB'd pillars (solid circles) in comparison with the annealed electroplated pillars (open circles) and (b) cross-section of a representative annealed electroplated pillar.

strengthening can be attributed to grain size effects. More recently, Böhm et al. [41] studied the uniaxial tensile properties of 40 nm-thick Au thin films deposited onto polyimide substrates and observed flow stresses as high as 500 MPa. It should be noted that these gold films are much thinner than any of the pillars tested in the present work and have extremely small grain sizes, unlike the single-crystalline pillars. The results of these previous studies clearly show strong size effects on strength even in the absence of strain gradients. While most of the thin film results cited here are usually interpreted in terms of dislocation confinement or grain size hardening, the effects of dislocation starvation described below might also be an important factor in controlling the thin film strength.

A prominent molecular dynamics study performed by Horstmeyer et al. [32] also reported a significant size effect in the absence of strain gradients. One of their discoveries was the presence of a strong inverse power relationship between the yield stress and the volume-to-surface-area ratio of a computational unit cell. In order to compare our results with these findings, it is useful to extract the flow stresses of the pillars at 2% strain, as the imperfect indenter loading precludes the determination of the yield stress more precisely. The shear stress resolved onto the $\langle 1\ 0\ -1 \rangle / \{1\ 1\ 1\}$ slip system at that flow stress is then calculated and normalized by the shear modulus in that slip system for a consistent data comparison. Both sets of normalized results of shear stress vs. volume/surface area (V/SA, which is the same as the pillar diameter in our case) are plotted in Fig. 9.

This comparison shows the power law predicted by the EAM modeling, as well as the non-power relationship of the experimental findings. The experimental data at pillar diameters greater than about 0.5 μm indicates that there might be a power law relation between the

yield shear stress and the volume/surface area ratio, as suggested by the EAM modeling, though the observed normalized strengths are significantly below the EAM predictions. The observed strengths for pillars with diameters below a critical value are much greater than can be predicted by the EAM modeling.

Since the results of our experiments indicate that the small cylindrical samples achieve very high strengths, it is useful to compare their behavior with that of whiskers. The size dependence of Cu whiskers, as shown by classic experiments of Brenner [43,44] was interpreted as early as 1947 by Fisher and Hollomon [45] and subsequently by many others, as indicating that these whiskers initially contained a small number of defects (dislocations). In typical whisker-like stress–strain behavior, the initial elastic loading leads to a very high critical stress, at which there is a significant drop in stress and a continued plastic flow at very low stresses. This high critical stress is associated with the nucleation of the first dislocations while the very low stresses during subsequent plasticity are a consequence of the high density of mobile dislocations inside the deformed whiskers. Retesting undeformed volumes causes the enormous initial yield stress to reappear because – analogously to the initial yielding – dislocation nucleation must occur before plastic flow can proceed. So, whisker-like plasticity is characterized by very high yield stresses followed by huge strain softening and flow at very small stresses. A typical graph representing whisker behavior in tension as well as the typical stress–strain curve we find for pillars is presented in Fig. 10. Unlike the whiskers, the stress–strain curve of the gold nanopillars is composed of elastic loading segments separated by discrete displacement bursts throughout the deformation without a significant reduction in the flow stress. This major difference between the whisker-like and the nanopillar behavior, that the flow stress does not fall to a low value following the strain burst, strongly suggests that the pillars may become dislocation starved just after each strain burst.

A possible explanation for these great strengths in uniaxial compression involves the concept of dislocation starvation. In ordinary plasticity dislocation motion leads to dislocation multiplication by double cross-slip and similar processes, which invariably leads to softening before strain hardening occurs through the elastic interaction of dislocations. For soft metals this leads to an increased dislocation density and strong Taylor hardening. However, unlike in bulk samples, dislocations inside of small crystals can only travel much smaller distances before annihilating at the free surface, thereby reducing the probability of multiplication processes. Indeed, Gilman's [46] description of dislocation multiplication leads naturally to a length scale for dislocation multiplication, δ, the distance a dislocation must travel before it replicates itself. From the table of multi-
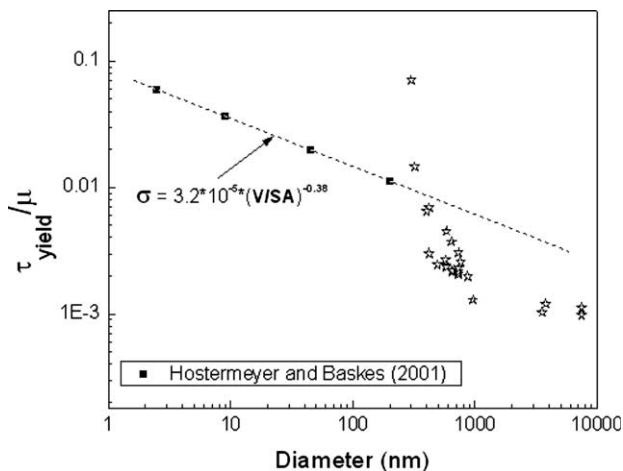

Fig. 9. Shear stress at 2% strain, or τ_y, normalized by $\langle 1\ 0\ -1 \rangle / \{1\ 1\ 1\}$ shear modulus vs. volume/surface area (same as diameter) of $\langle 0\ 0\ 1 \rangle$-oriented compressed FIB'd pillars plotted on log–log scale.
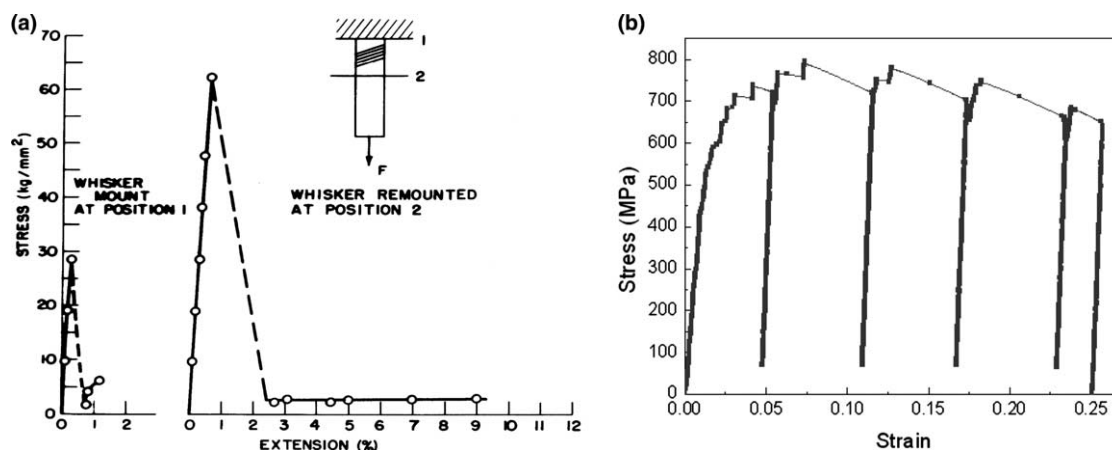
Fig. 10. (a) Stress–strain dependence of a Cu whisker in tension (Fisher and Hollomon, 1947); (b) stress–strain curve for a Au pillar in compression.

plication constants in Gilman's book, the length scale for multiplication for various metals can be estimated. For Ag it is of the order of 1 μm. This suggests that for silver, and perhaps gold, crystals smaller than this characteristic length might behave quite differently from bulk crystals. If the conditions for multiplication are not met, the dislocations would leave the small crystals before they have a chance to multiply, leading to dislocation starvation. These microscopic sample volumes, therefore, might inhibit multiplication of dislocations, creating a more favorable condition for them to leave the crystal at a nearby free surface. Once the dislocation-starved conditions are reached, very high stresses would be required to nucleate new dislocations, either at surfaces or in the bulk of the crystal, leading to the observed near-theoretical-strengths.

The proposed dislocation starvation model has not been fully developed at this point. Current efforts are focused on the TEM analysis of the thinned pillars before and after the deformation and observing the evolution of dislocations inside. This will serve as an important check for the proposed dislocation starvation model.

4.2. Summary

Uniaxial compression tests were conducted on single-crystalline, $\langle 0\,0\,1 \rangle$-oriented gold pillars of diameters varying between 300 and 7450 nm fabricated by the FIB technique. The results of these experiments indicate a strong sample size effect: the pillars yielded at stresses that are much higher than the typical yield strength of bulk gold of ~30 MPa at 2% strain [35]. Moreover, the flow stresses for the single-crystalline $\langle 0\,0\,1 \rangle$-oriented pillars reached 4.5 GPa, a significant fraction of the theoretical shear strength. An alternative, lithography-based microfabrication technique with subsequent gold electroplating was developed in order to address the possibility of Ga^+ implantation as a key contributor to the observed increase in flow stress. These annealed elec-

troplated pillars were found to exhibit a strong size effect, as well, supporting the proposed Dislocation Starvation model. Although this model is in the preliminary stages of its development, the data obtained for the 300 nm-diameter pillar matches the hypothesis of the initial escape of mobile dislocation followed by the state of dislocation starvation in the crystal. Subsequent nucleation of dislocations is thought to be required in order to accommodate further plasticity.

Acknowledgments

References

[1] Fleck NA, Muller GM, Ashby MF, Hutchinson JW. Acta Metall Mater 1994;42:475.
[2] Stolken JS, Evans AG. Acta Mater 1998;46:5109.
[3] Stelmashenko NA, Walls MG, Brown LM, Millman YV. Acta Metall Mater 1993;41:2855.
[4] De Guzman MS, Neubauer G, Flinn P, Nix WD. Mater Res Symp Proc 1993;308:613.
[5] Atkinson M. J Mater Res 1995;10:2908.
[6] Ma Q, Clarke DR. J Mater Res 1995;10:853.
[7] Poole WJ, Ashby MF, Fleck NA. Scr Metall Mater 1996;34:559.

[8] McElhaney KW, Vlassak JJ, Nix WD. J Mater Res 1998;13:1300.

[9] Suresh S, Nieh TG, Choi BW. Scr Mater 1999;41:951.

[10] Gerberich WW, Tymiak NI, et al. J Appl Mech – Trans ASME 2002;69:433–42.

[11] Nix WD, Gao H. J Mech Phys Solids 1998;46:411.

[12] Ashby MF. Philos Mag 1970;21:399.

[13] Gao H, Huang Y, Nix WD. Naturwissenschaftler 1999;86:507.

[14] Gao H, Huang Y, Nix WD, Hutchinson JW. J Mech Phys Solids 1999;47:1239.

[15] Huang Y, Gao H, Nix WD, Hutchinson JW. J Mech Phys Solids 2000;48:99.

[16] Huang Y, Xue Z, Gao H, Nix WD, Xia ZC. J Mater Res 2000;15:1786.

[17] Huang Y, Chen JY, Guo TF, Zhang L, Hwang KC. Int J Fract 1999;100:1–27.

[18] Pethica JB, Oliver WC. Proc Mater Res Soc 1988:13–23.

[19] Page TF, Oliver WC, McHargue CJ. J Mater Res 1992;7: 450–473.

[20] Gerberich WW, Nelson JC, Lilleodden ET, Anderson P, Wyrobek JT. Acta Mater 1996;44:3585–98.

[21] Mann AB, Pethica JB. Proc Mater Res Soc 1996:153–8.

[22] Corcoran SG, Colton RJ, Lilleodden ET, Gerberich WW. Phys Rev B 1997;55:16057–60.

[23] Kiely JD, Jarauch KF, Houston JE, Russell PE. J Mater Res 2000;15:1693–701.

[24] Suresh S, Nieh TG, Choi BW. Scr Mater 1999;41:951–7.

[25] Frank FC, van der Merwe JH. Proc Roy Soc (London) 1949;A198:216.

[26] Matthews JW, Blakeslee AE. J Cryst Growth 1974;27:118.

[27] Matthews JW, Blakeslee AE. J Cryst Growth 1975;34:265.

[28] Freund LB. J Appl Mech 1987;54:553.

[29] Nix WD. Metall Trans A 1989;20:2217.

[30] von Blanckenhagen B, Gumbsch P, Arzt E. Philos Mag Lett 2003;83:1–8.

[31] Arzt E, Dehm G, et al. Prog Mater Sci 2001;46:283–307.

[32] Horstemeyer MF, Baskes MI, Plimpton SJ. Acta Mater 2001;49:4363–74.

[33] Uchic MD, Dimiduk DM, Florando JN, Nix WD. Science 2004;305:986–9.

[34] Sneddon I. Int J Eng Sci 1965;3:47.

[35] Savitskii EM, Prince A. Handbook of precious metals. Hemisphere Publishing Company; 1969. p. 128–9.

[36] Arnold B, Lohse, Bauer H-D, Gemming T, Wetzig K, Binder K. Microsc Microanal 2003;9:140.

[37] Machalett F, Edinger K, Melngailis J, Diegel M, Steenbeck K, Steinbeiss E. Appl Phys A 2000;71:331–5.

[38] Yu DY, Spaepen F. J Appl Phys 2003;95:2991–7.

[39] Kraft O, Hommel M. Acta Mater 2001;49:3935–47.

[40] Huang H, Spaepen F. Acta Mater 2000;48:3261–9.

[41] Bohm J, Gruber P, Spolenak R, Stierle A, Wanner A, Arzt E. Rev Sci Instrum 2004;75:1110–9.

[42] Nix WD, Leung OS. In: Encyclopedia of materials: science and technology. Oxford: Pergamon; 2001. p. 9262–74.

[43] Brenner SS. J Appl Phys 1956;27:2218.

[44] Brenner SS, Doremus RH, Roberts BW, Turnbull D. Growth and Perfection of Crystals. New York: John Wiley; 1958. p. 157.

[45] Fisher J, Hollomon J. AIME 1947:2218.

[46] Gilman JJ. Appl Micromech Flow Solids 1953:185–90.